

Stabilized Maximum-Likelihood Iterative Quantum Amplitude Estimation for Structural CVaR under Correlated Random Fields

Alireza Tabarraei^{a,b,*}

^a*Department of Mechanical Engineering and Engineering Science, The University of North Carolina at Charlotte, Charlotte, NC 28223, USA*
^b*School of Data Science, The University of North Carolina at Charlotte, Charlotte, NC 28223, USA*

Abstract

Conditional Value-at-Risk (CVaR) is a fundamental tail-risk measure in stochastic structural mechanics, yet its accurate evaluation under high-dimensional, spatially correlated material uncertainty remains computationally prohibitive for classical Monte Carlo methods. Leveraging bounded-expectation reformulations of CVaR compatible with quantum amplitude estimation, we develop a quantum-enhanced inference framework that casts CVaR evaluation as a statistically consistent, confidence-constrained maximum-likelihood amplitude estimation problem. The proposed approach extends iterative quantum amplitude estimation (IQAE) by embedding explicit maximum-likelihood inference within a rigorously controlled interval-tracking architecture. To ensure global correctness under finite-shot noise and the non-injective oscillatory response induced by Grover amplification, we introduce a stabilized inference scheme incorporating multi-hypothesis feasibility tracking, periodic low-depth disambiguation, and a bounded restart mechanism governed by an explicit failure-probability budget. This hybrid likelihood–interval formulation preserves the quadratic oracle-complexity advantage of amplitude estimation while providing provable finite-sample confidence guarantees and substantially reduced estimator variance. The framework is demonstrated on examples with spatially correlated lognormal Young’s modulus fields generated via a Nyström low-rank Gaussian kernel model. Numerical experiments show that the proposed estimator achieves significantly lower oracle complexity than classical Monte Carlo CVaR estimation at comparable confidence levels, while maintaining rigorous global statistical reliability. This work establishes a practically robust and theoretically grounded quantum-enhanced methodology for tail-risk quantification in stochastic continuum mechanics and introduces a new class of confidence-constrained maximum-likelihood amplitude estimators for engineering uncertainty quantification.

Keywords: Iterative quantum amplitude estimation, Conditional value-at-risk (CVaR), structural reliability, quantum computing, Finite element analysis.

2010 MSC: 00-01, 99-00

1. Introduction

In computational mechanics, the quantification of structural response under uncertainty has become increasingly important as engineers seek to design systems that are not only efficient under nominal conditions but also resilient to variability in material properties, loads, and boundary conditions [1–4]. Traditional uncertainty quantification approaches in engineering have primarily focused on mean responses, variances, and failure probabilities derived from limit-state functions and reliability indices [5–7]. While these measures are

effective for characterizing average behavior and failure likelihood, they are often insufficient for assessing the severity of rare but consequential structural responses.

In many engineering applications, safety margins, serviceability limits, and certification decisions are governed by extreme responses rather than by central tendencies. Unusually large compliance, stress, displacement, or fatigue responses can dominate structural performance and lead to catastrophic failure, even when mean behavior remains acceptable [8, 9]. From a physical perspective, such extremes are frequently driven by localized failure mechanisms, including shear bands, cracks, and strain-softening zones, which generate highly concentrated stress fields and dominate the upper tail of the response distribution. These phenom-

*Corresponding author

Email address: atabarra@charlotte.edu (Alireza Tabarraei)

ena arise in impact, fracture, and failure of heterogeneous materials and have been extensively studied in computational mechanics [10–14]. Because these localized responses are rare but severe, they are poorly characterized by mean or variance alone, underscoring the need for tail-sensitive risk measures.

Among such measures, value-at-risk (VaR) and conditional value-at-risk (CVaR) have been extensively studied in finance, operations research, and risk management [15–18]. CVaR is particularly attractive due to its coherent and convex formulation, which quantifies tail severity by averaging responses beyond a prescribed quantile threshold. These properties have motivated growing interest in engineering and structural mechanics, where CVaR offers a principled compromise between robustness and tractability [19]. In contrast to worst-case formulations, which are often overly conservative and numerically unstable, CVaR preserves sensitivity to extreme responses while remaining amenable to analysis and optimization [4, 17]. Recent work has explored CVaR-based formulations for reliability assessment and risk-aware design under correlated uncertainty in structural systems, including surrogate-based strategies for estimating tail risk in nonlinear finite element models [19, 20].

Despite these attractive theoretical and practical features, accurate CVaR estimation remains computationally demanding. Naive Monte Carlo (MC) sampling requires a prohibitively large number of forward model evaluations to adequately resolve tail behavior, particularly as the confidence level approaches unity, rendering it impractical for high-fidelity finite element simulations [21]. This challenge has motivated the development of classical rare-event simulation and variance-reduction techniques aimed at concentrating computational effort in critical regions of the probability space. Representative approaches include importance sampling [5], subset simulation [22, 23], and surrogate-based response surface and polynomial chaos methods [24, 25]. While these methods can substantially improve efficiency relative to naive sampling, their performance may deteriorate for complex mechanics problems involving high-dimensional correlated random fields, nonlinear constitutive behavior, and computationally expensive finite element solvers [2, 26]. In particular, the generation of representative realizations of spatially correlated material fields using, for example, Karhunen–Loëve expansions [1, 3] or low-rank Gaussian process and Nyström kernel approximations [27, 28] requires careful numerical treatment to avoid prohibitive memory and computational costs. Consequently, even with advanced variance-reduction and surrogate modeling, the num-

ber of required forward simulations can remain prohibitively large for high-confidence CVaR estimation.

Quantum amplitude estimation (QAE) has emerged as a foundational quantum algorithmic primitive for the evaluation of bounded expectations and integrals, providing a provable asymptotic improvement in sampling complexity over classical Monte Carlo under the standard oracle query model [29–31]. In its seminal formulation, Brassard *et al.* [29] established amplitude amplification and amplitude estimation as quantum analogues of classical averaging and numerical integration, demonstrating that estimation error can scale inversely with the number of oracle queries rather than with its square root as in classical sampling. Subsequent complexity-theoretic analyses clarified the role of amplitude estimation as the quantum counterpart of Monte Carlo summation and integration and established matching lower bounds for broad classes of expectation estimation problems [30, 31]. These results positioned amplitude estimation as a central building block for quantum-accelerated uncertainty quantification and stochastic simulation.

The relevance of amplitude-estimation-based quantum algorithms to tail-sensitive risk measures has been explored primarily in financial and probabilistic modeling, where value-at-risk and conditional value-at-risk can be expressed as bounded hinge or loss expectations that are naturally compatible with amplitude estimation [32]. In this context, Woerner and Egger [32] formulated quantum algorithms for VaR and CVaR computation and demonstrated the asymptotic sampling-complexity advantages of amplitude estimation for risk analysis. Related quantum Monte Carlo approaches have further investigated expectation and tail-risk estimation for derivative pricing and probabilistic simulation using amplitude-estimation primitives [33–35]. These developments establish amplitude estimation as a theoretically powerful computational engine for tail-risk quantification.

Despite these asymptotic advantages, canonical amplitude estimation relies on quantum phase estimation and controlled Grover amplification [29, 36], resulting in deep circuits that are challenging to implement on near-term quantum hardware. This limitation has motivated the development of phase-estimation-free alternatives that trade modest classical post-processing for substantial reductions in circuit depth and qubit overhead [37]. Among these, iterative quantum amplitude estimation (IQAE) [38] has emerged as a particularly practical approach, replacing phase estimation with adaptive confidence-interval refinement based on repeated Grover amplification. Subsequent extensions have in-

troduced likelihood-based and Bayesian formulations to improve robustness under finite-shot noise and device imperfections [37, 39]. Nevertheless, existing IQAE variants typically rely on feasibility-based interval updates and fixed or heuristic probing schedules, which can exhibit instability in the presence of aliasing and finite-sample noise.

In parallel, there has been growing interest in applying quantum algorithms to problems in computational mechanics and structural reliability [40–42]. However, existing studies have largely focused on isolated algorithmic components or idealized demonstrations and have not yet established quantum workflows that couple realistic material uncertainty models with full finite element analyses. In particular, quantum treatments of spatially correlated random fields and their propagation through high-fidelity structural solvers remain largely unexplored. While foundational connections between quantum algorithms and the finite element method have been established in a theoretical setting [43], and recent work has investigated quantum-enhanced pipelines for data-driven mechanics, multiscale modeling, and topology optimization [41, 44, 45], the integration of amplitude-estimation-based inference with correlated material uncertainty and tail-risk objectives such as CVaR has not been systematically addressed. This gap motivates the present work.

In this work, we introduce a stabilized maximum-likelihood iterative quantum amplitude estimation (ML-IQAE) framework for CVaR estimation of structural responses under correlated random fields. ML-IQAE augments IQAE with likelihood-constrained interval tracking, adaptive Grover-depth and shot allocation, multi-hypothesis pruning, periodic low-depth disambiguation, and explicit failure-probability budgeting, providing statistically stable convergence under aliasing and finite-shot noise. We adopt a finite-scenario framework in which a low-rank Nyström approximation [27] is used to generate spatially correlated material modulus fields for one-dimensional and two-dimensional benchmark problems. Conditional on a fixed value-at-risk threshold determined from the scenario distribution, CVaR estimation reduces to the expectation of a normalized hinge function bounded in [0, 1], which naturally admits an amplitude estimation formulation [32].

We provide controlled comparisons against classical Monte Carlo under identical fixed VaR conditions and report absolute error as a function of oracle-call budget. All scenario responses are generated using full finite element solves under correlated random fields, and ML-IQAE operates on a lookup-table oracle constructed from these high-fidelity simulations. The re-

sults demonstrate that ML-IQAE exhibits sub-classical sampling complexity in practice, consistent with the asymptotic convergence guarantees of amplitude estimation [29, 38]. By integrating mechanics-relevant uncertainty models with a mechanically grounded CVaR formulation and stabilized likelihood-constrained amplitude estimation, this work establishes a systematic benchmark at the intersection of computational mechanics, structural reliability, and quantum algorithms, and provides a structured baseline for future studies of quantum-accelerated tail-risk estimation in engineering.

2. Problem formulation and reduction of CVaR estimation to amplitude estimation

2.1. Stochastic finite element formulation

Let $\mathbf{x} \in \Omega \subset \mathbb{R}^d$ denote the spatial coordinate in the structural domain with boundary $\partial\Omega = \Gamma_u \cup \Gamma_t$, where Γ_u and Γ_t are the Dirichlet and Neumann boundaries, respectively. The stochastic linear elasticity problem seeks a displacement field $\mathbf{u}(\mathbf{x}, \omega) \in \mathbb{R}^d$ satisfying

$$-\nabla \cdot (\mathbf{C}(\mathbf{x}, \omega) : \nabla^s \mathbf{u}(\mathbf{x}, \omega)) = \mathbf{f}(\mathbf{x}), \quad \mathbf{x} \in \Omega, \quad (1)$$

with boundary conditions $\mathbf{u} = \mathbf{0}$ on Γ_u and $\sigma(\mathbf{u}) \mathbf{n} = \mathbf{t}$ on Γ_t . Here $\mathbf{C}(\mathbf{x}, \omega)$ denotes the random fourth-order elasticity tensor, $\nabla^s(\cdot)$ is the symmetric gradient operator, σ is the Cauchy stress tensor, \mathbf{n} is the outward unit normal on Γ_t , and $\mathbf{f}(\mathbf{x})$ and $\mathbf{t}(\mathbf{x})$ denote prescribed body forces and surface tractions, respectively. The random parameter ω is defined on the probability space $(\Xi, \mathcal{F}, \mathbb{P})$, where Ξ is the sample space, \mathcal{F} is the associated σ -algebra, and \mathbb{P} is the probability measure.

A conforming finite element discretization yields the stochastic linear system

$$\mathbf{K}(\omega) \mathbf{u}(\omega) = \mathbf{f}, \quad (2)$$

where $\mathbf{K}(\omega) \in \mathbb{R}^{N \times N}$ is the random global stiffness matrix assembled from element-level contributions, $\mathbf{u}(\omega) \in \mathbb{R}^N$ is the vector of nodal displacements, and $\mathbf{f} \in \mathbb{R}^N$ is the deterministic global load vector. For each realization, a scalar structural performance quantity of interest (QoI), such as the compliance, stress or displacement, is computed.

2.1.1. Nyström low-rank representation of correlated random fields

The stochastic elasticity tensor $\mathbf{C}(\mathbf{x}, \omega)$ is modeled through a spatially correlated lognormal random field

for the Young's modulus $E(\mathbf{x}, \omega)$. Specifically, we assume that the log-modulus field admits the representation

$$\log E(\mathbf{x}, \omega) = \sigma \sum_{j=1}^r \phi_j(\mathbf{x}) \xi_j(\omega), \quad (3)$$

where $\{\xi_j\}_{j=1}^r$ are independent standard normal random variables and $\{\phi_j(\mathbf{x})\}$ form a truncated low-rank spatial basis obtained from a Nyström approximation of a Gaussian kernel covariance operator.

Let $k(\mathbf{x}, \mathbf{x}')$ denote the anisotropic Gaussian covariance kernel

$$k(\mathbf{x}, \mathbf{x}') = \exp\left(-\frac{1}{2} \left[\left(\frac{x_1 - x'_1}{\ell_x} \right)^2 + \left(\frac{x_2 - x'_2}{\ell_y} \right)^2 \right]\right). \quad (4)$$

Given a set of spatial sampling points $\{\mathbf{x}_m\}_{m=1}^M$, the Nyström method constructs a low-rank approximation of the kernel operator by eigen-decomposition of the matrix $K_{MM} = [k(\mathbf{x}_m, \mathbf{x}_n)]$ and yields the approximate eigenfunctions

$$\phi_j(\mathbf{x}) \approx \sum_{m=1}^M k(\mathbf{x}, \mathbf{x}_m) \frac{u_{mj}}{\sqrt{\lambda_j}}, \quad j = 1, \dots, r, \quad (5)$$

where λ_j and u_{mj} are eigenpairs of K_{MM} .

This representation enables efficient sampling of high-dimensional correlated random fields using only $r \ll N$ latent variables while preserving spatial correlation structure compatible with the finite element discretization. Each realization ω_i therefore corresponds to a vector $\xi^{(i)} \in \mathbb{R}^r$ which induces a deterministic Young's modulus field $E(\mathbf{x}, \omega_i)$ and hence a deterministic stiffness matrix $\mathbf{K}(\omega_i)$.

2.2. Tail-risk measures

Let $Q(\omega)$ denote a real-valued random structural response. The value-at-risk (VaR) at confidence level $\alpha \in (0, 1)$ is defined as the lower α -quantile of the response distribution [15, 18]

$$\eta_\alpha = \inf \{\eta \in \mathbb{R} : \mathbb{P}(Q(\omega) \leq \eta) \geq \alpha\}. \quad (6)$$

The conditional value-at-risk (CVaR), also referred to as the expected shortfall, measures the expected severity of responses exceeding the VaR threshold and is defined as [16, 17]

$$\text{CVaR}_\alpha(Q) = \mathbb{E}[Q(\omega) | Q(\omega) \geq \eta_\alpha]. \quad (7)$$

An equivalent convex optimization-based characterization of CVaR is given by [15, 17]

$$\text{CVaR}_\alpha(Q) = \min_{\eta \in \mathbb{R}} \left\{ \eta + \frac{1}{1-\alpha} \mathbb{E}[(Q(\omega) - \eta)_+] \right\}, \quad (8)$$

where $(x)_+ = \max(x, 0)$ denotes the positive part operator.

2.3. Discrete scenario formulation

To enable computational treatment, the continuous probability space is approximated by a finite discrete scenario set

$$\{(\omega_i, p_i)\}_{i=1}^{N_s}, \quad p_i > 0, \quad \sum_{i=1}^{N_s} p_i = 1, \quad (9)$$

where ω_i denotes a realization of the underlying random field and p_i is the associated probability weight. The corresponding structural responses are denoted by

$$Q_i = Q(\omega_i), \quad i = 1, \dots, N_s. \quad (10)$$

Let $\{Q_{(i)}\}$ denote the ordered response values such that

$$Q_{(1)} \leq Q_{(2)} \leq \dots \leq Q_{(N_s)}, \quad (11)$$

with reordered probabilities $\{p_{(i)}\}$. The discrete value-at-risk at confidence level α is then defined as the smallest response level satisfying

$$\sum_{j=1}^{k_\alpha} p_{(j)} \geq \alpha, \quad (12)$$

and is given by

$$\eta_\alpha = Q_{(k_\alpha)}, \quad (13)$$

where

$$k_\alpha = \min \left\{ k : \sum_{j=1}^k p_{(j)} \geq \alpha \right\}. \quad (14)$$

Using this discrete VaR threshold, the conditional value-at-risk is expressed as

$$\text{CVaR}_\alpha(Q) = \eta_\alpha + \frac{1}{1-\alpha} \sum_{i=1}^{N_s} p_i \max(Q_i - \eta_\alpha, 0), \quad (15)$$

which is a discrete realization of the optimization-based CVaR representation.

2.4. Reduction of CVaR to a bounded expectation

Equation (15) shows that CVaR estimation reduces to computing the expectation of a hinge function of the structural response. Quantum amplitude estimation is naturally suited to estimating expectations of bounded random variables. To bring the discrete CVaR formulation into a form compatible with amplitude estimation, following the normalization strategy introduced in quantum risk analysis [32, 33], we define normalized hinge variables

$$g_i = \frac{\max(Q_i - \eta_\alpha, 0)}{Q_{\max} - \eta_\alpha}, \quad Q_{\max} = \max_i Q_i, \quad (16)$$

which satisfy $g_i \in [0, 1]$. The normalized expectation

$$a = \sum_{i=1}^{N_s} p_i g_i = \mathbb{E}[g(\omega)] \quad (17)$$

can be directly encoded as a quantum amplitude and estimated via amplitude estimation.

The original CVaR is then recovered by the affine transformation

$$\text{CVaR}_\alpha(Q) = \eta_\alpha + \frac{Q_{\max} - \eta_\alpha}{1 - \alpha} a, \quad (18)$$

so that CVaR estimation reduces to the quantum estimation of a bounded expectation $a \in [0, 1]$.

3. Quantum algorithm for CVaR estimation

It was shown in Eq. (17) that CVaR estimation for the stochastic finite element model reduces to the computation of a single bounded expectation $a \in [0, 1]$. This quantity represents the normalized expected contribution of tail responses beyond the value-at-risk threshold and fully determines the desired conditional value-at-risk through an affine transformation. Consequently, the sole objective of the quantum algorithm developed in this work is to estimate the scalar parameter a with high accuracy using as few effective evaluations of the underlying stochastic model as possible.

Iterative quantum amplitude estimation (IQAE) provides a principled quantum inference framework for this task. Classical Monte Carlo estimates a by repeatedly sampling realizations of $g(\omega)$ and forming an empirical average, which leads to an estimation error that decays only at a rate proportional to the inverse square root of the number of samples. In contrast, quantum amplitude estimation exploits coherent quantum superposition and interference to encode the entire discrete probability distribution into a single quantum state, enabling estimation of bounded expectations with a mean-square error that scales inversely with the number of oracle queries under the standard quantum query model [29, 31]. This quadratic improvement in sampling complexity positions amplitude estimation as the quantum analogue of classical Monte Carlo integration and summation [30].

IQAE is a hardware-efficient reformulation of canonical amplitude estimation that avoids quantum phase estimation and deep controlled-unitary constructions, replacing them with an adaptive classical interval inference procedure driven by repeated Grover-type amplifications and projective measurements [38]. In the present context, IQAE operates by first embedding

the discrete normalized tail-response values $\{g_i\}$ into a quantum state via a state-preparation oracle that coherently represents all stochastic scenarios and their associated probabilities. A Grover amplification operator is then applied iteratively to rotate the quantum state within a low-dimensional invariant subspace, systematically amplifying the probability amplitude associated with the desired expectation parameter a . By performing measurements at different amplification depths and combining the resulting statistics using rigorous confidence interval constructions, IQAE progressively refines a feasible set for a while maintaining robustness to finite-shot noise and measurement uncertainty.

The structure and physical interpretation of the oracle construction and the Grover amplification operator are detailed in the following subsections.

3.1. Oracle construction

The role of the oracle in quantum amplitude estimation is to prepare a quantum state in which a target bounded expectation appears explicitly as the probability of a measurable binary event. In contrast to Boolean decision oracles, the oracle employed here is a *state-preparation oracle* that encodes real-valued information into quantum probability amplitudes.

In the present setting, the objective is to estimate the scalar expectation

$$a = \sum_{i=1}^{N_s} p_i g_i, \quad (19)$$

where $\{g_i\}_{i=1}^{N_s}$ are normalized tail-response values and $\{p_i\}_{i=1}^{N_s}$ are the corresponding scenario probabilities.

Let N_s denote the number of discrete stochastic scenarios and let

$$n = \lceil \log_2 N_s \rceil \quad (20)$$

be the number of qubits required to index them. The oracle is implemented as a unitary operator A acting on n index qubits and one ancilla qubit, constructed such that

$$A |0\rangle = \sum_{i=1}^{N_s} \sqrt{p_i} |i\rangle (\sqrt{1 - g_i} |0\rangle + \sqrt{g_i} |1\rangle). \quad (21)$$

Measuring the ancilla qubit yields outcome $|1\rangle$ with probability

$$\Pr(\text{ancilla} = 1) = a, \quad (22)$$

so that estimation of the expectation a reduces to inference of a single quantum measurement probability.

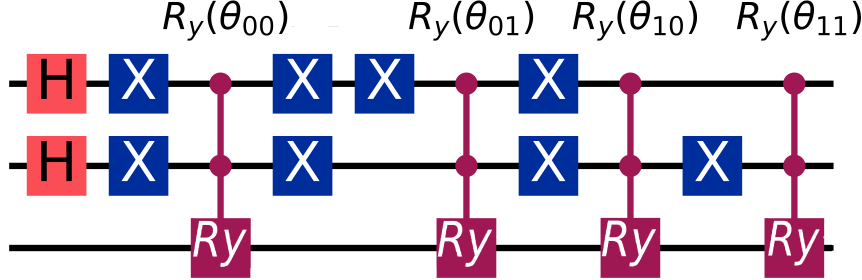


Figure 1: Oracle- A circuit used in this work to encode scenario-dependent values g_i into ancilla amplitudes via scenario-controlled R_y rotations. Pattern conversions required for controls-on- $|0\rangle$ are implemented using surrounding X gates, yielding a compact “lookup-table” implementation.

Define the projectors

$$\Pi_1 = I \otimes |1\rangle\langle 1|, \quad \Pi_0 = I \otimes |0\rangle\langle 0|. \quad (23)$$

Then

$$a = \langle 0| A^\dagger \Pi_1 A |0\rangle, \quad (24)$$

and the oracle-prepared state $|\Psi\rangle = A|0\rangle$ admits the orthogonal decomposition

$$|\Psi\rangle = \sqrt{1-a} |\psi_0\rangle + \sqrt{a} |\psi_1\rangle, \quad (25)$$

where

$$|\psi_1\rangle = \frac{\Pi_1 |\Psi\rangle}{\sqrt{a}}, \quad |\psi_0\rangle = \frac{\Pi_0 |\Psi\rangle}{\sqrt{1-a}}. \quad (26)$$

Introducing a global angle $\theta \in (0, \pi/2)$ such that

$$\sin^2 \theta = a = \sum_{i=1}^{N_s} p_i g_i, \quad (27)$$

the oracle action can be written compactly as

$$A|0\rangle = \cos \theta |\psi_0\rangle + \sin \theta |\psi_1\rangle. \quad (28)$$

Equation (28) defines the two-dimensional invariant subspace

$$\mathcal{K} = \text{span}\{|\psi_0\rangle, |\psi_1\rangle\}, \quad (29)$$

within which all Grover amplification dynamics take place.

3.1.1. Circuit-level realization and gate-level encoding

Figure 1 illustrates the circuit realization of the oracle A . In general, the oracle acts on an n -qubit index register together with a single ancilla qubit. For clarity and concreteness, Fig. 1 depicts the construction for a two-qubit index register, corresponding to four discrete scenarios, with the ancilla implemented as qubit 2. The index qubits encode the scenario label, while the ancilla

qubit is used to store the amplitude information required for quantum amplitude estimation.

The oracle circuit implements a conditional amplitude-encoding mechanism in which the normalized scenario-dependent values $\{g_i\}_{i=1}^{N_s}$ are mapped to the probability of measuring the ancilla qubit in state $|1\rangle$. This is achieved by applying scenario-controlled single-qubit rotations to the ancilla qubit, conditioned on the computational basis state of the index register.

For each scenario i , the oracle applies a controlled rotation $R_y(\phi_i)$ to the ancilla qubit, where the R_y gate is defined by the matrix

$$R_y(\phi_i) = \begin{pmatrix} \cos(\phi_i/2) & -\sin(\phi_i/2) \\ \sin(\phi_i/2) & \cos(\phi_i/2) \end{pmatrix}. \quad (30)$$

When acting on the ancilla state $|0\rangle$, this rotation produces the superposition

$$R_y(\phi_i)|0\rangle = \cos(\phi_i/2)|0\rangle + \sin(\phi_i/2)|1\rangle. \quad (31)$$

By the Born measurement rule, measuring the ancilla qubit then yields outcome $|1\rangle$ with probability

$$\Pr(\text{ancilla} = 1 \mid i) = \sin^2(\phi_i/2). \quad (32)$$

Accordingly, the rotation angles are chosen such that

$$\sin^2(\phi_i/2) = g_i, \quad (33)$$

ensuring that the ancilla measurement probability reproduces the prescribed normalized response value for scenario i .

The rotations $R_y(\phi_i)$ are implemented as multi-controlled operations in which the index qubits serve as controls and the ancilla qubit is the target. Each rotation is designed to act only when the index register is in a specific computational basis state corresponding to scenario i . Since standard controlled gates activate on control qubits in the $|1\rangle$ state, controls on $|0\rangle$ are realized

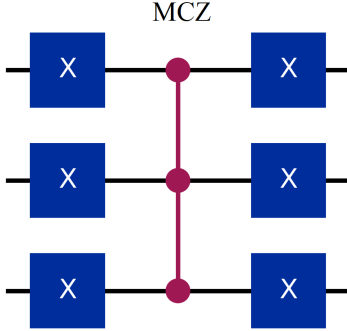


Figure 2: Circuit implementation of the reflection $S_0 = I - 2|000\rangle\langle 000|$ using Pauli- X conjugation of a multi-controlled Z gate.

by temporarily applying Pauli- X gates to the relevant index qubits before and after the controlled rotation. This control-pattern conversion ensures that exactly one basis state of the index register activates each ancilla rotation, while the index register is restored to its original configuration after the operation.

Taken together, the circuit realizes a coherent lookup-table oracle; each basis state of the index register activates a specific ancilla rotation that encodes the associated value g_i . When the index register is prepared in a superposition, all such controlled rotations act coherently, producing the oracle state in Eq. (21). We emphasize that the rotation angles $\{\phi_i\}$ are gate-level parameters used solely for local amplitude encoding within the circuit and are distinct from the global amplitude-estimation angle θ defined by $\sin^2 \theta = a$, which governs the subsequent Grover amplification dynamics.

3.2. Grover amplification

Grover amplification [29, 31, 36, 46] exploits the two-dimensional invariant subspace \mathcal{K} defined in Eq. (29) to perform deterministic and reversible rotations that amplify information associated with the unknown amplitude-estimation angle θ . When restricted to this subspace, the algorithm admits a geometric interpretation in terms of successive reflections that coherently rotate the oracle-prepared state toward the success subspace associated with the ancilla measurement outcome.

The two reflection operators underlying Grover amplification are

$$S_\chi = I - 2|\psi_1\rangle\langle\psi_1|, \quad S_0 = I - 2|0\rangle\langle 0|, \quad (34)$$

where S_χ implements a reflection about the success subspace spanned by $|\psi_1\rangle$ and S_0 implements a reflection about the all-zero computational basis state. In the

present setting, success is defined by observing the ancilla qubit in state $|1\rangle$, and S_χ therefore acts as a selective phase flip on all basis states with ancilla bit equal to one. At the circuit level, this operation is realized by a single Pauli- Z gate acting on the ancilla qubit, which introduces a π phase shift on all computational basis states with ancilla value $|1\rangle$.

The reflection S_0 is realized as a multi-controlled phase flip that applies a π phase shift exclusively to the computational basis state $|0\rangle^{\otimes(n+1)}$, where the additional qubit corresponds to the ancilla. As illustrated in Fig. 2, this operation is implemented by first applying Pauli- X gates to all qubits to map $|0\rangle$ to $|1\rangle^{\otimes(n+1)}$, followed by a multi-controlled Z (MCZ) gate, and finally uncomputing the basis transformation with a second layer of Pauli- X gates. The resulting action satisfies

$$|0\rangle \mapsto -|0\rangle, \quad |x\rangle \mapsto |x\rangle, \quad x \neq 0,$$

which is precisely the defining action of S_0 .

Combining the two reflections with the oracle A , the Grover iterate is defined as

$$G = -AS_0A^\dagger S_\chi. \quad (35)$$

A circuit-level realization of this operator, including the implementations of both S_χ and S_0 , is shown in Fig. 3.

Restricted to the invariant subspace \mathcal{K} , the Grover operator acts as a planar rotation by angle 2θ . After k Grover iterations, the state evolves according to

$$G^k A |0\rangle = \cos((2k+1)\theta) |\psi_0\rangle + \sin((2k+1)\theta) |\psi_1\rangle, \quad (36)$$

where $|\psi_0\rangle$ and $|\psi_1\rangle$ denote the orthogonal components of the oracle-prepared state within \mathcal{K} . Consequently, the probability of observing the ancilla qubit in the success state after k Grover iterations is

$$p_k(\theta) = \sin^2((2k+1)\theta). \quad (37)$$

Equations (36) and (37) show that Grover amplification transforms estimation of the static expectation value $a = \sin^2 \theta$ into estimation of the oscillation frequency θ . Interval-based quantum amplitude estimation leverages this deterministic oscillatory structure to infer a from amplified measurement statistics while maintaining rigorous finite-sample confidence guarantees.

4. Iterative quantum amplitude estimation for CVaR inference

Rather than estimating the unknown rotation angle θ via quantum phase estimation, which requires deep

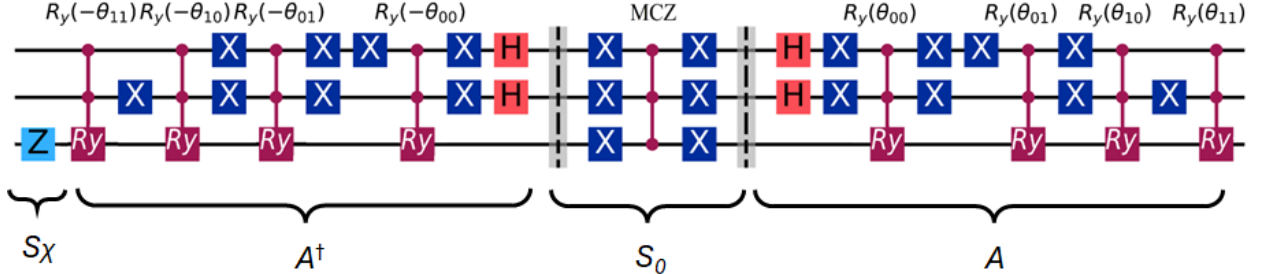


Figure 3: Quantum circuit for one Grover amplification step $G = -AS_0A^\dagger S_\chi$. The circuit consists of the success reflection S_χ , the inverse oracle A^\dagger , the zero-state reflection S_0 implemented with a multi-controlled Z gate, and the oracle A .

controlled-unitary circuits and additional ancilla qubits and forms the basis of the original amplitude estimation algorithm introduced by Brassard et al.[29], we employ iterative quantum amplitude estimation (IQAE) [37, 38]. IQAE avoids the quantum Fourier transform and phase estimation entirely, instead using carefully selected Grover amplification and classical post-processing to infer the amplitude from repeated measurements with rigorous confidence bounds. This approach significantly reduces the depth and qubit requirements compared to phase-estimation-based methods while retaining near-optimal query complexity.

At amplification depth k , the amplified quantum state

$$|\psi_k\rangle = G^k A |0\rangle \quad (38)$$

is prepared and measured multiple times. The probability of observing the ancilla in the success state is given by Eq. (37). By collecting measurement statistics across multiple amplification depths, IQAE progressively restricts the set of admissible parameter values that are statistically consistent with the observed data.

Throughout the IQAE procedure, we prescribe a global failure tolerance $\delta_{\text{tot}} \in (0, 1)$ that bounds the probability that the maintained admissible parameter set ever excludes the true rotation angle θ due to finite-shot statistical fluctuations. All per-round confidence allocations and disambiguation steps introduced below are constructed such that the overall probability of incorrectly excluding the true parameter satisfies

$$\Pr(\theta \notin \Theta^{(t)} \text{ for some } t) \leq \delta_{\text{tot}}.$$

This global tolerance serves as the primary confidence parameter governing the statistical reliability of the entire inference procedure and underpins the confidence-constrained estimation framework developed in the subsequent sections.

4.1. Measurement model and likelihood

Grover amplification maps the bounded expectation $a = \sin^2 \theta$ to the oscillatory success probability $p_k(\theta)$ given in Eq. (37). Estimating CVaR therefore, reduces to statistical inference of the unknown rotation angle θ from ancilla measurements of amplified quantum states.

At IQAE round t , an amplification depth k_t is selected and the amplified state $G^{k_t} A |0\rangle$ is executed m_t times. Each execution produces a Bernoulli outcome

$$Y_{t,i} \sim \text{Bernoulli}(p_{k_t}(\theta)), \quad i = 1, \dots, m_t,$$

where $Y_{t,i} = 1$ corresponds to observing the ancilla in the success state $|1\rangle$. Let $h_t = \sum_{i=1}^{m_t} Y_{t,i}$ denote the number of observed successes at round t . Then

$$h_t \sim \text{Binomial}(m_t, p_{k_t}(\theta)), \quad \hat{p}_{k_t} = \frac{h_t}{m_t}.$$

Let

$$\mathcal{D}_t = \{(k_j, m_j, h_j)\}_{j=1}^t \quad (39)$$

denote the measurement data collected up to and including round t . Assuming independent state preparations and measurements across rounds, the likelihood of the unknown parameter θ given \mathcal{D}_t is

$$\mathcal{L}(\theta; \mathcal{D}_t) = \prod_{j=1}^t \binom{m_j}{h_j} [p_{k_j}(\theta)]^{h_j} [1 - p_{k_j}(\theta)]^{m_j - h_j}. \quad (40)$$

Equation (40) casts IQAE as a nonlinear binomial regression problem in which θ is inferred from noisy observations of the response family $\{p_k(\theta)\}_{k \geq 0}$.

The online likelihood model (40) is operationalized by the adaptive interval-based procedure summarized in Algorithm 1. The resulting interval updates, hypothesis management and periodic disambiguation are developed in the subsequent subsections.

Algorithm 1 Structure of one ML-IQAE round t (feasibility update and MLE point estimate)

- 1: Select Grover depth k_t based on the current admissible set $\Theta^{(t-1)}$.
- 2: Select number of shots m_t subject to remaining oracle-call budget.
- 3: Execute the amplified circuit m_t times at depth k_t .
- 4: Record the number of observed successes h_t .
- 5: Allocate local confidence budget δ_t via Eq. (49).
- 6: Construct a Clopper–Pearson confidence interval for $p_{k_t}(\theta)$.
- 7: Update admissible parameter sets $\Theta^{(t)}$ via interval intersection (with pruning to M_{\max} components).
- 8: Apply disambiguation or restart logic if $\Theta^{(t)} = \emptyset$.
- 9: Update point estimate: compute $\hat{\theta}_t = \arg \max_{\theta \in \Theta^{(t)}} \ell(\theta; D_t)$ and $\hat{a}_t = \sin^2 \hat{\theta}_t$.

4.1.1. Maximum-likelihood estimation within admissible hypotheses

The interval-based inference procedure described above maintains a union of admissible parameter intervals $\Theta^{(t)} \subset (0, \pi/2)$ that contains the true rotation angle θ with prescribed global confidence. While this feasible set provides rigorous uncertainty certification, point estimation of θ within this set is required to obtain a sharp estimator for the underlying amplitude $a = \sin^2 \theta$.

Given the accumulated measurement data D_t , we define the log-likelihood function induced by the binomial observation model Eq. (40) as

$$\ell(\theta; D_t) = \sum_{j=1}^t [h_j \log p_{k_j}(\theta) + (m_j - h_j) \log(1 - p_{k_j}(\theta))], \quad (41)$$

where $p_k(\theta) = \sin^2((2k + 1)\theta)$.

The reported estimate of the rotation angle is defined as the constrained maximum-likelihood estimator

$$\hat{\theta}_t = \arg \max_{\theta \in \Theta^{(t)}} \ell(\theta; D_t), \quad (42)$$

with the corresponding amplitude estimate

$$\hat{a}_t = \sin^2 \hat{\theta}_t. \quad (43)$$

The admissible set $\Theta^{(t)}$ acts as a statistically valid feasibility constraint, ensuring that the true parameter θ is excluded only with probability at most δ_{tot} , while the maximum-likelihood criterion selects the most probable parameter value consistent with the accumulated data. This hybrid confidence-constrained formulation combines the global correctness guarantees of interval-based IQAE with the asymptotic efficiency and low-variance properties of maximum-likelihood estimation.

Consequently, the proposed estimator constitutes a confidence-constrained maximum-likelihood amplitude estimator, rather than a purely feasibility-based IQAE interval midpoint rule. This distinction is fundamental to the improved convergence behavior and variance reduction observed in the numerical experiments reported in Section 5.

4.2. Interval-based feasibility tracking with hypothesis management and disambiguation

The proposed ML-IQAE framework employs an interval-based feasibility-tracking procedure that progressively constructs a confidence-consistent admissible region for the unknown rotation angle θ . At each round, a new batch of amplified measurements is acquired at a selected Grover depth, converted into a binomial confidence interval for the corresponding success probability, and mapped into an admissible set of θ values. These admissible sets are intersected with previously retained constraints to form a global feasible region that serves as a statistically valid confidence certificate for the true parameter value.

Due to the oscillatory and non-injective structure of the response function $p_k(\theta) = \sin^2((2k + 1)\theta)$, the feasible region may consist of multiple disconnected components that are simultaneously consistent with the accumulated data. ML-IQAE therefore maintains a union of disjoint admissible intervals, referred to as hypotheses, and updates them sequentially as new measurements arrive. Spurious hypotheses are periodically pruned using low-depth disambiguation measurements, while rare empty-set events are handled through the controlled restart mechanism.

Since ML-IQAE proceeds sequentially under a finite quantum computational budget, we quantify cost directly in the query model by explicitly accounting for oracle invocations. At round t , the algorithm selects an amplification depth k_t and performs m_t shots of the amplified circuit $G^{k_t} A |0\rangle$. Each shot applies the Grover iterate G exactly k_t times and includes one initial application of A , so the oracle-call cost of round t is

$$C_t = (2k_t + 1)m_t. \quad (44)$$

If the run terminates after T rounds, the total oracle usage satisfies

$$\sum_{t=1}^T C_t \leq B. \quad (45)$$

Algorithm 1 summarizes the feasibility-update procedure with hypothesis management that provides the confidence-constrained admissible region used by the

maximum-likelihood estimator defined in Section 4.1.1. The following subsections formalize its main components: (i) binomial confidence-interval inference that maps each measurement batch into admissible sets for θ , (ii) multi-hypothesis tracking to represent disconnected feasible regions, and (iii) periodic low-depth disambiguation for pruning spurious modes.

All confidence intervals used by ML-IQAE are constructed under a global summable risk allocation $\{\delta_t\}_{t \geq 1}$ satisfying $\sum_{t \geq 1} \delta_t \leq \delta_{\text{tot}}$, which guarantees global correctness under adaptive measurement and hypothesis pruning. The formal construction is given in Section 4.2.2.

4.2.1. Binomial confidence bounds for amplified measurements

At each round t , ML-IQAE converts the observed success count h_t from m_t amplified measurements into a statistically valid confidence interval for the corresponding success probability $p_{k_t}(\theta)$. To ensure exact, non-asymptotic coverage under finite sampling and adaptive measurement selection, we employ the classical Clopper–Pearson construction [47, 48].

Given a prescribed per-round failure tolerance δ_t , the Clopper–Pearson confidence interval $[p_L^{(t)}, p_U^{(t)}]$ is defined by

$$p_L^{(t)} = I_{\delta_t/2}^{-1}(h_t, m_t - h_t + 1), \quad p_U^{(t)} = I_{1-\delta_t/2}^{-1}(h_t + 1, m_t - h_t), \quad (46)$$

Here $I_q^{-1}(a, b)$ denotes the inverse of the regularized incomplete beta function [49, 50], which arises naturally from inversion of the binomial distribution in the Clopper–Pearson construction [48]. This interval satisfies the exact coverage guarantee

$$\Pr(p_{k_t}(\theta) \in [p_L^{(t)}, p_U^{(t)}]) \geq 1 - \delta_t, \quad (47)$$

independently of the sample size m_t and without asymptotic assumptions.

The resulting probability interval $[p_L^{(t)}, p_U^{(t)}]$ is subsequently mapped into an admissible parameter set Θ_{k_t} through the response relation $p_{k_t}(\theta) = \sin^2((2k_t + 1)\theta)$, as formalized in Section 4.2.2.

4.2.2. Core interval inference

Let $\delta_{\text{tot}} \in (0, 1)$ denote the prescribed overall failure tolerance for a single ML-IQAE run. We allocate a per-round risk budget δ_t such that

$$\sum_{t=1}^{\infty} \delta_t \leq \delta_{\text{tot}}. \quad (48)$$

In this work we employ the summable schedule

$$\delta_t = \frac{6}{\pi^2} \frac{\delta_{\text{tot}}}{t^2}, \quad (49)$$

which satisfies (48). All binomial confidence intervals used by ML-IQAE are constructed with per-round coverage at least $1 - \delta_t$.

For the batch $(k_t, m_t, h_t) \in \mathcal{D}_t$, the empirical success frequency $\hat{p}_{k_t} = h_t/m_t$ estimates the response probability $p_{k_t}(\theta)$ in (37). A confidence interval $[p_L, p_U]$ is constructed using the exact Clopper–Pearson method [47, 48] such that

$$\Pr(p_{k_t}(\theta) \in [p_L, p_U]) \geq 1 - \delta_t. \quad (50)$$

where $[p_L, p_U]$ is computed from (m_t, h_t) . The induced admissible parameter set is

$$\Theta_{k_t} = \{\theta \in (0, \pi/2) : p_{k_t}(\theta) \in [p_L, p_U]\}, \quad (51)$$

which serves as a confidence-consistent feasibility constraint for the maximum-likelihood estimator defined in Section 4.1.1.

After t rounds, the globally admissible region is

$$\Theta^{(t)} = \bigcap_{j=1}^t \Theta_{k_j}, \quad (52)$$

which constitutes a confidence-certified feasible region for θ . For reporting uncertainty bounds, we also maintain the convex hull

$$[\theta_L^{(t)}, \theta_U^{(t)}] = \text{hull}(\Theta^{(t)}). \quad (53)$$

By a union bound, the maintained hull interval satisfies

$$\Pr(\theta \in [\theta_L^{(t)}, \theta_U^{(t)}]) \geq 1 - \sum_{j=1}^t \delta_{k_j}. \quad (54)$$

4.2.3. Adaptive selection of Grover depth

At each round t , the Grover amplification depth k_t is chosen adaptively based on the current admissible region $\Theta^{(t-1)}$ and the accumulated measurement data. A provisional point estimate $\hat{\theta}_{t-1}$ is first obtained by maximum-likelihood inference over $\Theta^{(t-1)}$, and a nominal amplification depth is computed using the standard information-optimal probing condition of quantum amplitude estimation [29, 37, 38]

$$k_{\text{prop}} = \left\lfloor \frac{\pi}{8\hat{\theta}_{t-1}} - \frac{1}{2} \right\rfloor. \quad (55)$$

To prevent aliasing and loss of statistical identifiability due to the periodic and non-injective structure of

$p_k(\theta) = \sin^2((2k+1)\theta)$, we impose the alias-safety condition

$$(2k_t + 1)\theta_U^{(t-1)} \leq \kappa, \quad \kappa = 0.49\pi, \quad (56)$$

which guarantees that $p_k(\theta)$ remains strictly monotone over the entire admissible region. This yields the corresponding safety bound

$$k_{\text{safe}} = \left\lfloor \frac{\kappa}{2\theta_U^{(t-1)}} - \frac{1}{2} \right\rfloor. \quad (57)$$

The final depth is then selected as

$$k_t = \min\{k_{\text{prop}}, k_{\text{safe}}, k_{\text{max}}, k_{t-1} + 1\}, \quad (58)$$

where k_{max} is a prescribed upper bound and the monotonicity constraint $k_t \leq k_{t-1} + 1$ prevents abrupt jumps that could destabilize the inference. In addition, if successive empirical success frequencies approach saturation near 0 or 1, the algorithm temporarily reduces k_t to avoid degenerate binomial observations. This adaptive policy concentrates oracle calls at statistically informative amplification depths while preserving global robustness.

At each round t , the number of measurement shots m_t is selected adaptively to balance statistical accuracy with overall oracle-call efficiency. Because the binomial confidence interval width scales as $O(m_t^{-1/2})$, increasing m_t improves the precision of the induced admissible region Θ_t , but excessive shot counts at early rounds are inefficient when the feasible region is still wide.

ML-IQAE therefore employs a gradually increasing shot policy in which m_t is chosen as a smooth function of the remaining oracle-call budget and the current round index. This strategy allocates relatively few shots at early rounds to obtain coarse but informative constraints, and progressively increases m_t as the admissible region contracts and higher resolution is required. The shot count is additionally capped by the remaining budget and a prescribed minimum to ensure that each batch provides a statistically meaningful update while avoiding premature budget exhaustion.

More precisely, ML-IQAE employs the budget-aware shot allocation rule

$$m_t = \min\{m_t^{(1)}, m_t^{(2)}\}, \quad m_{\min} \leq m_t \leq m_{\max}, \quad (59)$$

with

$$m_t^{(1)} = \bar{m}(B)(1 + \alpha t), \quad (60a)$$

$$m_t^{(2)} = \frac{B - \sum_{j < t} (2k_j + 1)m_j}{(2k_t + 1)R_t}. \quad (60b)$$

where B is the total oracle-call budget, $\bar{m}(B) = \Theta(B^{1/4})$ is a smooth base shot scale, $\alpha > 0$ is a small growth rate, and R_t is a prescribed lower bound on the remaining number of rounds. The first term increases the nominal shot count gradually as the inference progresses, while the second term ensures that sufficient budget is retained to complete the remaining rounds. The bounds m_{\min} and m_{\max} guarantee that each batch yields a statistically meaningful update while preventing premature budget exhaustion.

In the present implementation we choose

$$\bar{m}(B) = 220B^{1/4}, \quad (61a)$$

$$\alpha = 0.012, \quad (61b)$$

$$R_t = \max\{10, 28 - \min(t, 20)\}, \quad (61c)$$

and clip m_t to $m_{\min} \leq m_t \leq m_{\max}$ with $m_{\min} = 50$ and $m_{\max} = 1100$. These values provide stable early-stage exploration, smooth precision refinement at later rounds, and reliable suppression of spurious admissible modes during disambiguation.

4.2.4. Adaptive shot allocation

This adaptive shot-allocation policy concentrates oracle calls at statistically informative stages of the inference, improves the stability of likelihood-based pruning, and contributes significantly to the observed reduction in oracle complexity relative to classical Monte Carlo estimation.

4.2.5. Multi-hypothesis management

Because $p_k(\theta) = \sin^2((2k+1)\theta)$ is non-injective, the admissible region $\Theta^{(t)}$ may become disconnected and consist of multiple disjoint subintervals that are simultaneously consistent with the accumulated data. We therefore represent the confidence-consistent feasible region using a finite hypothesis set

$$\mathcal{H}^{(t)} = \{\Theta_1^{(t)}, \dots, \Theta_{M_t}^{(t)}\}, \quad (62)$$

where each $\Theta_m^{(t)}$ is a disjoint admissible interval that serves as a candidate feasible domain for the maximum-likelihood estimator defined in Section 4.1.1.

When a new batch $(k_{t+1}, m_{t+1}, h_{t+1})$ is acquired, each hypothesis is updated by intersection,

$$\Theta_m^{(t+1)} = \Theta_m^{(t)} \cap \Theta_{k_{t+1}}, \quad m = 1, \dots, M_t, \quad (63)$$

and empty hypotheses are discarded. To prevent combinatorial growth, only the M_{\max} surviving hypotheses with the largest attained likelihood values $\max_{\theta \in \Theta_m^{(t)}} \ell(\theta; D_t)$ are retained, which prioritizes statistically dominant feasible modes rather than purely geometric interval width.

Algorithm 2 High-level ML-IQAE iteration with union-of-intervals feasible sets

Require: Initial feasible set $\Theta^{(0)} \subset (0, \pi/2)$ represented as a union of disjoint intervals; global failure tolerance δ_{tot} ; oracle-call budget B .

Ensure: Final feasible set $\Theta^{(T)}$ (union of intervals) and an estimate of $a = \sin^2 \theta$ (or failure).

- 1: $t \leftarrow 1$.
- 2: **while** budget remains and stopping criterion not met **do**
- 3: Choose Grover depth k_t based on the current feasible set $\Theta^{(t-1)}$.
- 4: Choose shots m_t subject to remaining budget (cost $\propto (2k_t + 1)m_t$).
- 5: Run the amplified circuit m_t times at depth k_t and record successes h_t .
- 6: Allocate per-round risk $\delta_t \leftarrow \delta_{\text{schedule}}(t, \delta_{\text{tot}}) \triangleright$ Eq. (49)
- 7: Define the round- t success probability $p_t(\theta) = \sin^2((2k_t + 1)\theta)$.
- 8: Build a binomial confidence interval $[p_L^{(t)}, p_U^{(t)}]$ for $p_t(\theta)$ (Clopper–Pearson).
- 9: Convert $[p_L^{(t)}, p_U^{(t)}]$ into a feasible set for θ :
$$\Theta_t = \{\theta \in (0, \pi/2) : p_t(\theta) \in [p_L^{(t)}, p_U^{(t)}]\}.$$
- 10: Update the global feasible set by intersection:
$$\Theta^{(t)} \leftarrow \Theta^{(t-1)} \cap \Theta_t.$$
- 11: Represent $\Theta^{(t)}$ as a union of disjoint intervals and apply likelihood-based hypothesis pruning (keep at most M_{max} components).
- 12: **if** a disambiguation step is scheduled **then**
- 13: Acquire additional low-depth batches (e.g., $k \in \{0, 1, 2\}$ with larger shot counts) and update $\Theta^{(t)}$ as above.
- 14: **end if**
- 15: Update point estimate:
$$\hat{\theta}_t = \arg \max_{\theta \in \Theta^{(t)}} \ell(\theta; D_t) \text{ and } \hat{a}_t = \sin^2 \hat{\theta}_t.$$
- 16: $t \leftarrow t + 1$.
- 17: **end while**
- 18: **return** $\Theta^{(T)}$ and \hat{a}_T (or $a \in [\sin^2(\theta_L^{(T)}), \sin^2(\theta_U^{(T)})]$ if only bounds are desired).

4.2.6. Periodic disambiguation

The oscillatory and non-injective structure of the inverse response $p_k(\theta) = \sin^2((2k + 1)\theta)$ implies that, as higher amplification depths are employed, the admissible parameter set may fracture into multiple disconnected components that are simultaneously compat-

ible with the accumulated interval constraints. Many of these components correspond to alias modes introduced by the periodicity of the sine function rather than to statistically supported parameter values.

To eliminate such spurious modes, the ML-IQAE framework periodically (e.g., after every 5 rounds) re-estimates low-depth response probabilities using a significantly increased number of shots over a fixed low-depth set

$$\mathcal{K}_{\text{dis}} = \{0, 1, 2\}.$$

These high-fidelity low-frequency measurements tighten the corresponding confidence intervals and impose strong global constraints on θ that rapidly invalidate alias components that are only weakly consistent with the accumulated data.

For each active hypothesis $\Theta_m^{(t)}$, the refined admissible region is obtained by intersecting with the high-precision disambiguation constraints,

$$\Theta_{m,k}^{(t+1)} = \Theta_m^{(t)} \cap \Theta_k, \quad k \in \mathcal{K}_{\text{dis}},$$

followed by likelihood-based pruning of the resulting hypothesis set as described in Section 4.2.5. This periodic disambiguation mechanism is a key component of the proposed ML-IQAE framework and is not present in classical IQAE formulations [38].

To ensure robustness, a bounded restart-on-empty mechanism is employed. If an update causes the feasible parameter set to collapse due to finite-shot noise or aliasing, the most recent observation is discarded and the inference state is reconstructed from earlier consistent measurements. A small number of additional low-depth samples are then used to reinitialize the admissible region. This process is strictly bounded and guarantees recovery without biasing the final estimate.

The complete stabilized ML-IQAE procedure, including likelihood-based hypothesis tracking and periodic disambiguation is summarized in Algorithm 2. An example of the oracle construction and circuit implementation are provided in Appendix A.

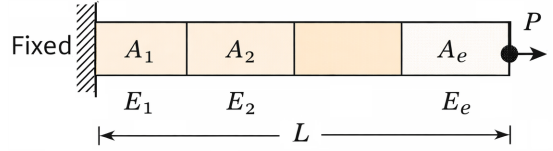


Figure 4: 1D axial bar benchmark. Left end fixed ($u(0) = 0$) and point load P applied at $x = L$. The bar is discretized into linear elements with constant properties.

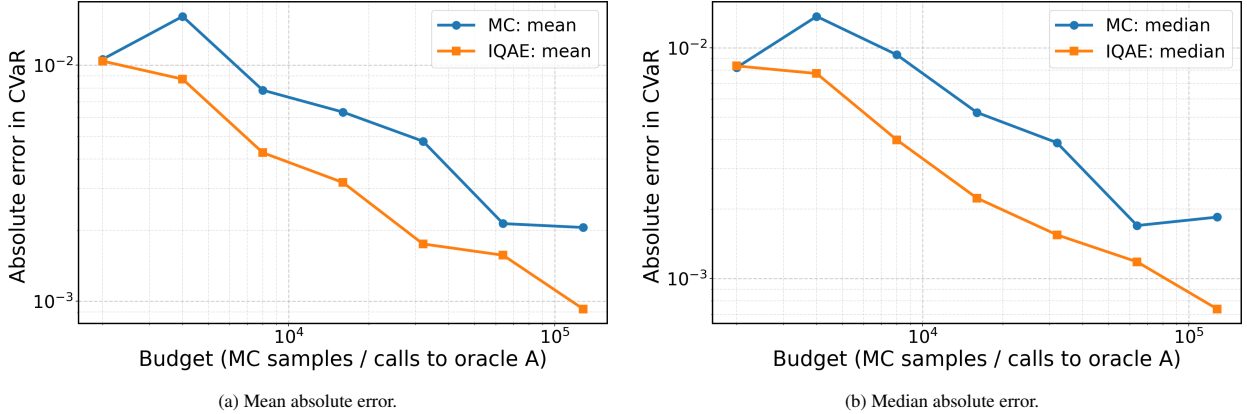


Figure 5: Absolute error in $\text{CVaR}_\alpha(Q)$ for compliance $Q = C$ of the bar benchmark versus requested compute budget.

Table 1: Standard deviation of the absolute CVaR_α error across repeated runs for the 1D axial bar problem with compliance as the quantity of interest.

Budget	MC Std	IQAE Std
2000	1.03e-2	6.40e-3
4000	1.19e-2	4.92e-3
8000	4.80e-3	3.07e-3
16000	4.16e-3	2.55e-3
32000	2.77e-3	1.31e-3
64000	2.01e-3	2.10e-3
128000	1.50e-3	8.94e-4

5. Numerical Benchmarks

This section presents a sequence of numerical benchmarks designed to assess the performance of the proposed stabilized ML-IQAE framework for CVaR estimation in stochastic structural mechanics. The examples progress from a one-dimensional axial bar with discrete material uncertainty to two-dimensional cantilever and L-bracket problems with spatially correlated random fields. This hierarchy allows us to isolate estimator behavior from geometric complexity and progressively examine performance under increasing mechanical and statistical challenges.

5.1. 1D axial bar benchmark (discrete random field)

To isolate estimator behavior from geometric complexity, we consider a one-dimensional axial bar of length L discretized into $n_e = 20$ linear finite elements. The left end of the bar is fixed, $u(0) = 0$, and a point load P is applied at the right end, $x = L$ (Figure 4). This configuration admits a closed and interpretable relationship between the response and the applied load, making it a convenient baseline for assessing risk-aware estimators.

Material uncertainty is introduced through a discrete random field defined element-wise. Each element is assigned a Young's modulus E_e drawn independently from a finite set of 15 admissible levels, resulting in a collection of stochastic realizations with associated probabilities $\{p_i\}$. For this benchmark, we evaluate tail risk using the conditional value-at-risk CVaR_α at confidence level $\alpha = 0.95$.

We consider compliance as the quantity of interest, defined as

$$Q = C = P u(L),$$

where $u(L)$ denotes the tip displacement. For a single point load, compliance is proportional to the tip displacement, and therefore both quantities induce identical stochastic orderings and risk measures up to a constant scaling factor. For this reason, we report results only for compliance, noting that the same conclusions apply to the tip displacement.

Figure 5 reports the absolute error in $\text{CVaR}_\alpha(Q)$ as a function of the requested compute budget, interpreted as either the number of Monte Carlo samples or the number of calls to oracle A for the IQAE-based estimator. The mean absolute error curves reflect average estimator performance across repeated runs, while the median curves provide a more robust characterization of typical behavior by reducing sensitivity to rare but high-error realizations.

At low budgets, MC and IQAE exhibit comparable mean errors, although MC displays larger fluctuations due to sampling variability. As the budget increases, IQAE consistently achieves lower errors and exhibits a steeper decay rate. This improvement is particularly pronounced in the median error curves, where IQAE maintains substantially smaller errors across the full range of budgets, indicating more reliable convergence

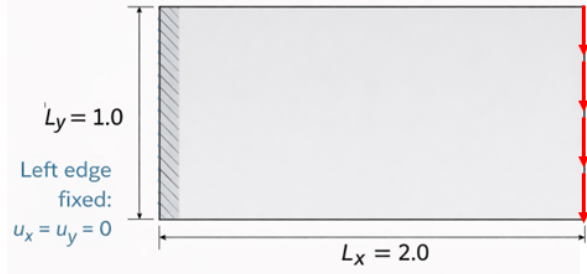


Figure 6: Two-dimensional cantilever beam benchmark. The beam has length $L_x = 2.0$ and height $L_y = 1.0$. The left edge is fully clamped, and a vertical traction load is applied along the right edge.

and fewer extreme outliers.

The variability across runs is quantified by the standard deviation of the absolute CVaR error, reported in Table 1. In this context, the standard deviation measures the spread of estimation errors across independent repetitions at a fixed budget and thus characterizes estimator stability rather than bias. Larger standard deviations indicate a higher likelihood of sporadic large errors, even if the mean performance appears acceptable. Consistent with the error curves, MC exhibits larger standard deviations, reflecting sensitivity to tail events and sampling noise. IQAE generally maintains smaller standard deviations, particularly at moderate and high budgets, indicating a more concentrated error distribution. Overall, this simple 1D benchmark confirms that IQAE provides not only improved average accuracy but also enhanced robustness in estimating tail risk.

5.2. Cantilever Beam Benchmark

We next consider a two-dimensional cantilever beam benchmark under plane stress conditions. The geometry, boundary conditions, and loading configuration are shown in Fig. 6. The beam is discretized using bilinear quadrilateral (Q4) finite elements. The left boundary is fully clamped, enforcing zero displacement in both spatial directions, while a uniform vertical traction load is applied along the right edge.

Material uncertainty is introduced through a spatially correlated random field for the Young's modulus. The correlation structure is defined by a Gaussian-process prior and implemented using a low-rank Nyström approximation, as described in Section 2.1.1. This construction enforces smooth spatial variability in material stiffness across the domain while enabling efficient sampling of stochastic realizations. The continuous random field is discretized into a finite ensemble of stochastic realizations with associated probabilities, which are used consistently by both Monte Carlo and IQAE-based estimators.

For this benchmark, we evaluate the conditional value-at-risk CVaR $_{\alpha}$ at confidence level $\alpha = 0.95$ for three quantities of interest computed from the same finite element solutions: (i) structural compliance, (ii) vertical tip displacement measured at the mid-height of the free edge, and (iii) the maximum von Mises stress over all elements. For each QoI, CVaR is estimated using standard Monte Carlo sampling and the proposed IQAE-based estimator. The absolute estimation error is reported as a function of the requested computational budget, interpreted as the number of MC samples or the number of calls to oracle A .

Figure 7 shows the CVaR estimation error for compliance. Both MC and IQAE exhibit decreasing mean and median errors as the computational budget increases, indicating convergence for both estimators. However, IQAE consistently achieves lower error at comparable

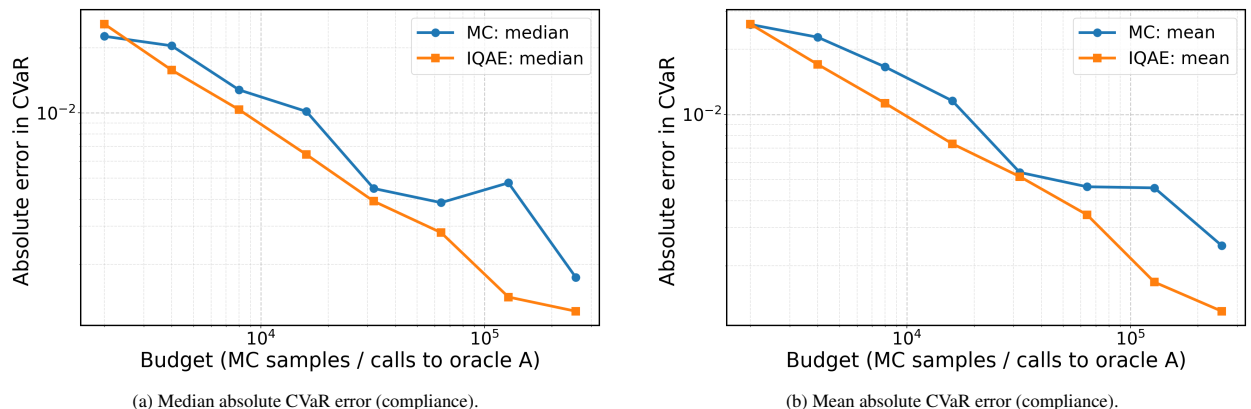


Figure 7: Absolute error in CVaR $_{\alpha}$ estimation of structural compliance for the cantilever beam benchmark as a function of the computational budget.

budgets. The separation between the median curves is particularly pronounced, highlighting that IQAE yields more reliable performance across repeated runs and is less affected by occasional high-error realizations that inflate the mean error for Monte Carlo sampling.

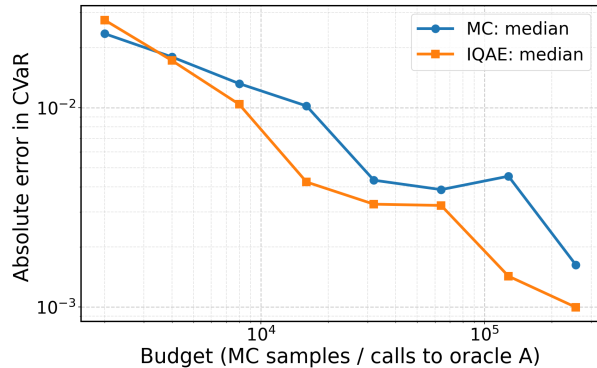
The corresponding results for the vertical tip displacement are reported in Fig. 8. The same qualitative trends are observed: IQAE provides a faster decay of both mean and median CVaR error compared to MC, with the advantage becoming more pronounced at moderate and high budgets. This behavior reflects the improved efficiency of amplitude-estimation-based sampling for displacement-driven quantities, which are sensitive to rare but influential material realizations in the upper tail of the response distribution.

Figure 9 presents the CVaR estimation error for the maximum von Mises stress. Stress-based QoIs exhibit highly skewed and heavy-tailed distributions, mak-

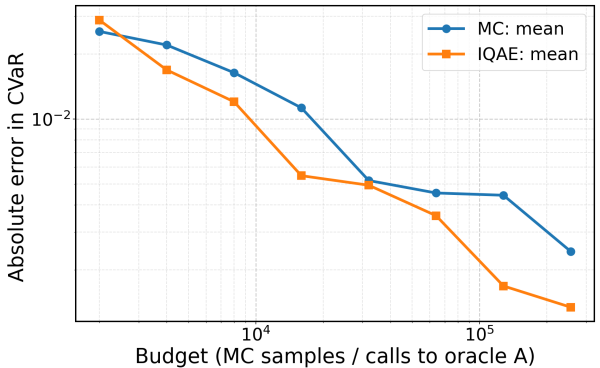
ing accurate tail estimation particularly challenging for naive Monte Carlo sampling. In this regime, IQAE substantially outperforms MC across all tested budgets, achieving significantly lower mean and median errors. The improvement is especially pronounced at higher budgets, where IQAE continues to reduce error while MC convergence slows due to persistent tail variance.

To quantify estimator robustness, Table 2 reports the standard deviation of the absolute CVaR error across repeated runs for all three quantities of interest. Across compliance and displacement, IQAE generally exhibits lower or comparable variability relative to MC, with a clear advantage at higher budgets. For the maximum von Mises stress, where response distributions are strongly heavy-tailed, IQAE achieves a substantial reduction in variability over most budgets, underscoring its effectiveness for stress-driven risk metrics.

Overall, the cantilever beam benchmark demon-

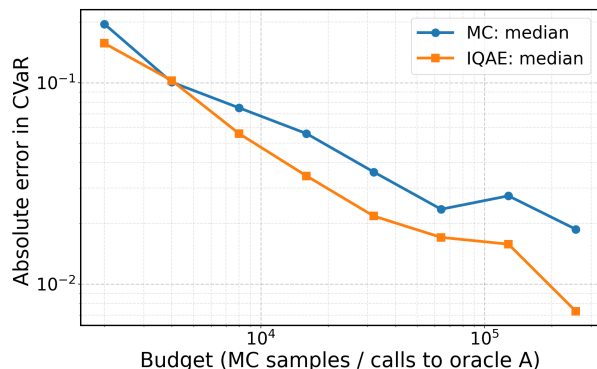


(a) Median absolute CVaR error (tip displacement).

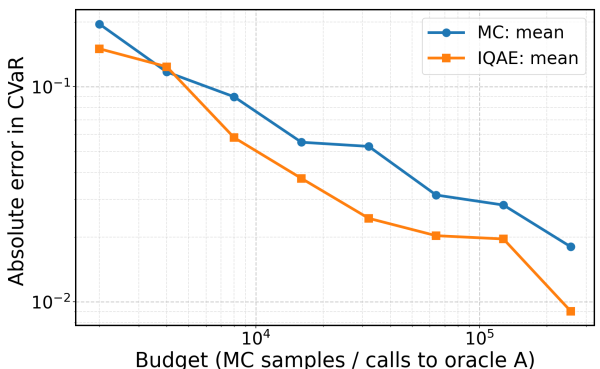


(b) Mean absolute CVaR error (tip displacement).

Figure 8: Absolute error in CVaR_α estimation of vertical tip displacement for the cantilever beam benchmark as a function of the computational budget.



(a) Median absolute CVaR error (max von Mises stress).



(b) Mean absolute CVaR error (max von Mises stress).

Figure 9: Absolute error in CVaR_α estimation of the maximum von Mises stress for the cantilever beam benchmark as a function of the computational budget.

Table 2: Standard deviation of the absolute CVaR $_{\alpha}$ error across repeated runs for the 2D cantilever problem. Results are shown for Monte Carlo and IQAE estimators across all three quantities of interest.

Budget	Compliance		Tip displacement		Max von Mises stress	
	MC	IQAE	MC	IQAE	MC	IQAE
2000	1.82e-2	2.12e-2	1.73e-2	1.72e-2	1.71e-1	9.06e-2
4000	1.43e-2	9.85e-3	1.41e-2	1.05e-2	1.12e-1	7.67e-2
8000	1.24e-2	8.27e-3	1.23e-2	9.48e-3	6.28e-2	3.76e-2
16000	8.13e-3	5.17e-3	7.95e-3	4.21e-3	3.06e-2	2.66e-2
32000	4.95e-3	4.75e-3	4.90e-3	4.22e-3	4.51e-2	1.87e-2
64000	3.56e-3	2.91e-3	3.48e-3	2.57e-3	2.55e-2	1.52e-2
128000	3.31e-3	1.30e-3	3.23e-3	1.35e-3	1.71e-2	4.29e-2
256000	1.87e-3	1.22e-3	1.82e-3	1.17e-3	1.33e-2	7.42e-3

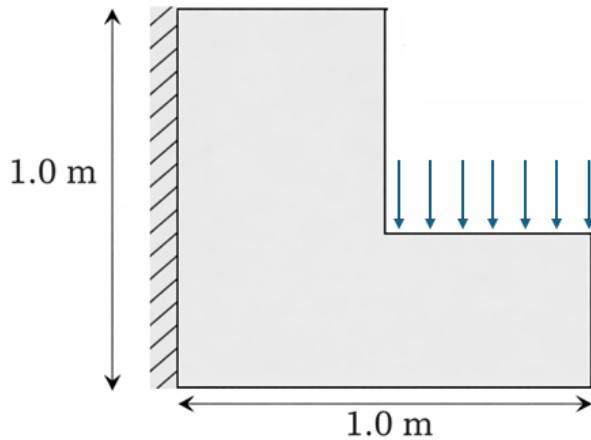


Figure 10: Geometry and boundary conditions of the L-shaped benchmark domain.

strates that IQAE delivers consistent accuracy gains and improved robustness over Monte Carlo sampling across compliance-, displacement-, and stress-based CVaR metrics. These improvements are achieved without problem-specific tuning and persist under spatially correlated material uncertainty, highlighting the generality and practical relevance of the proposed approach for risk-aware structural analysis.

5.3. L-bracket benchmark: stress-based CVaR under correlated material uncertainty

The L-bracket benchmark is used to assess the performance of the proposed stabilized ML-IQAE framework in a mechanically demanding setting characterized by geometric singularities and pronounced stress localization. As shown in Fig. 10, the re-entrant corner of the L-shaped domain induces a classical stress singularity, resulting in highly concentrated von Mises stress fields near the corner. This feature makes the upper tail of the

stress response distribution particularly sensitive to spatially correlated material fluctuations and therefore provides a stringent test for stress-based CVaR estimation under limited computational budgets.

The problem is formulated under plane-stress conditions with uncertainty introduced through a spatially correlated, lognormal Young's modulus field. The same Gaussian-process-based correlation model employed in the cantilever benchmark is used here, with realizations generated via a Nyström low-rank approximation of the covariance kernel. A fixed discrete scenario ensemble is constructed, and the conditional value-at-risk of the maximum von Mises stress, CVaR $_{0.95}(\sigma_{\text{vm},\text{max}})$, is evaluated. As in the previous benchmarks, the value-at-risk threshold is computed once from the full scenario distribution and held fixed throughout the estimation process, so that both Monte Carlo and ML-IQAE estimate the same normalized hinge expectation. This design isolates the effect of the inference strategy and enables a direct comparison of oracle efficiency.

Figure 11(a) reports the median absolute CVaR error as a function of the requested oracle-call budget. The median is used to characterize typical estimator performance under the highly skewed error distributions associated with tail-dominated stress responses. Across all tested budgets, Monte Carlo exhibits slow convergence, while ML-IQAE consistently achieves lower median error once moderate budgets are available. The performance gap widens as the budget increases, indicating that ML-IQAE resolves the stress-driven tail behavior more efficiently than independent sampling. This improvement is particularly significant in this benchmark, where rare high-stress events dominate the CVaR metric. To complement the median statistics, Fig. 11(b) shows the mean absolute CVaR error without variance shading. The mean trends closely mirror the median behavior, confirming that the observed improvement is

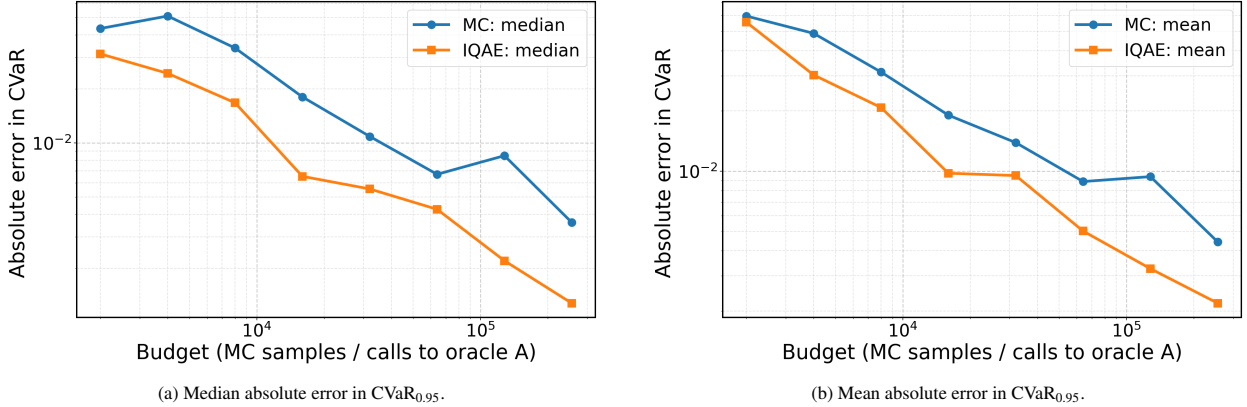


Figure 11: Stress-based CVaR estimation for the L-bracket benchmark under spatially correlated material uncertainty. The quantity of interest is the conditional value-at-risk of the maximum von Mises stress over the domain. Results compare Monte Carlo sampling with the proposed IQAE-based estimator as a function of the total oracle-call budget.

not driven by a small number of favorable realizations. In particular, ML-IQAE maintains a lower mean error than Monte Carlo over the full range of tested budgets and exhibits a visibly steeper decay rate at higher budgets, consistent with the improved oracle complexity of amplitude-estimation-based inference.

The robustness of the two estimators is quantified in Table 3, which reports the standard deviation of the absolute CVaR error across repeated runs. Monte Carlo exhibits substantial variability due to the difficulty of consistently sampling rare, high-stress realizations associated with the re-entrant corner. In contrast, ML-IQAE demonstrates a systematically reduced standard deviation at moderate and high budgets, indicating a tighter concentration of estimator outcomes. This variance reduction reflects the stabilizing effect of likelihood-based hypothesis management and periodic low-depth disambiguation, which suppress aliasing and finite-shot noise in the amplified response.

At the lowest budgets, ML-IQAE can exhibit variability comparable to Monte Carlo. This behavior is expected given the oscillatory and non-injective nature of the amplified response function and the limited sta-

tistical information available in this regime. However, as additional oracle calls are allocated, the admissible parameter region contracts rapidly, spurious hypotheses are eliminated, and the estimator transitions into a stable convergence regime with reduced dispersion.

Importantly, no ML-IQAE run failed for this benchmark across any tested budget. The empirical failure rate is therefore zero, confirming that the bounded restart-on-empty mechanism is effective even in the presence of severe stress localization and tail sensitivity. This result underscores the practical robustness of the stabilized inference framework and its suitability for mechanically realistic CVaR estimation problems.

Overall, the L-bracket results demonstrate that ML-IQAE provides a reliable and sample-efficient alternative to classical Monte Carlo sampling for stress-based CVaR estimation in geometrically complex structures. The method achieves lower typical and average errors, exhibits reduced estimator variance, and maintains strict robustness guarantees without incurring failures, even under challenging tail-dominated conditions.

6. Conclusions

This work presented a stabilized inference framework for risk-aware structural analysis based on iterative quantum amplitude estimation. The proposed ML-IQAE approach targets the efficient and robust estimation of conditional value-at-risk for quantities of interest arising in finite-element models with spatially correlated material uncertainty. By combining likelihood-based hypothesis management, periodic low-depth disambiguation, and a bounded restart-on-empty mechanism, the framework addresses key practical challenges

Table 3: Standard deviation of the absolute CVaR _{α} error across repeated runs for the L-bracket problem with maximum von Mises stress as the quantity of interest.

Budget	MC Std	IQAE Std
2000	5.10e-2	5.19e-2
4000	3.46e-2	2.60e-2
8000	2.23e-2	2.10e-2
16000	1.73e-2	1.49e-2
32000	1.10e-2	9.36e-3

that arise when applying amplitude-estimation-based methods to mechanically realistic problems.

The performance of the proposed method was evaluated across three progressively challenging benchmarks: a one-dimensional axial bar, a two-dimensional cantilever beam, and a stress-dominated L-bracket problem with a re-entrant corner. In all cases, material uncertainty was modeled using spatially correlated random fields constructed from Gaussian-process priors, ensuring physically meaningful variability while preserving computational tractability. For each benchmark, CVaR was evaluated at a fixed confidence level using identical scenario ensembles, enabling a direct comparison between classical Monte Carlo sampling and ML-IQAE under equivalent oracle-call budgets.

Across all benchmarks and quantities of interest, ML-IQAE consistently achieved lower median and mean absolute CVaR errors than Monte Carlo sampling once moderate budgets were available. These gains were most pronounced for stress-based quantities, where heavy-tailed response distributions and localized singularities severely limit the effectiveness of independent sampling. In such regimes, ML-IQAE demonstrated markedly faster error decay and substantially reduced estimator variance, highlighting its ability to focus computational effort on the tail events that dominate CVaR.

In addition to accuracy improvements, the proposed framework exhibited strong robustness properties. Variance across repeated runs was consistently reduced relative to Monte Carlo, particularly at higher budgets, and no inference failures were observed in any benchmark. This confirms that the stabilization mechanisms incorporated into ML-IQAE are effective in suppressing aliasing, finite-shot noise, and spurious hypothesis persistence, even in the presence of highly skewed and non-smooth response distributions.

Overall, the results demonstrate that ML-IQAE provides a reliable and sample-efficient alternative to classical Monte Carlo methods for CVaR estimation in structural mechanics under correlated material uncertainty. The framework is fully compatible with existing finite-element solvers and does not require problem-specific tuning, making it a promising foundation for future quantum-enhanced risk-aware analysis and design workflows. As quantum hardware and fault-tolerant implementations mature, the proposed approach offers a clear pathway for integrating quantum inference primitives into large-scale computational mechanics applications.

7. Acknowledgments

The author acknowledges the financial support of the National Science Foundation under Award No. CMMI-2527378.

References

- [1] R. Ghanem, P. Spanos, *Stochastic finite elements: a spectral approach*, Springer-Verlag, 1991.
- [2] O. Le Maître, O. Knio, *Spectral Methods for Uncertainty Quantification: With Applications to Computational Fluid Dynamics*, Springer, 2010.
- [3] D. Xiu, *Numerical Methods for Stochastic Computations: A Spectral Method Approach*, Princeton University Press, 2010.
- [4] R. C. Smith, *Uncertainty quantification: theory, implementation, and applications*, SIAM, 2024.
- [5] R. E. Melchers, A. T. Beck, *Structural reliability analysis and prediction*, John wiley & sons, 2018.
- [6] H. O. Madsen, S. Krenk, N. C. Lind, *Methods of structural safety*, Courier Corporation, 2006.
- [7] A. Der Kiureghian, *Structural reliability methods for seismic safety assessment: a review*, *Engineering structures* 18 (6) (1996) 412–424.
- [8] A. S. Nowak, K. R. Collins, *Reliability of structures*, CRC press, 2012.
- [9] A. H.-S. Ang, W. H. Tang, *Probability Concepts in Engineering: Emphasis on Applications to Civil and Environmental Engineering*, Wiley, 2007.
- [10] Z. P. Bažant, B. H. Oh, *Crack band theory for fracture of concrete*, *Materials and Structures* 16 (3) (1983) 155–177.
- [11] M. S. Elapolu, A. Tabarraei, *Mechanical and fracture properties of polycrystalline graphene with hydrogenated grain boundaries*, *The Journal of Physical Chemistry C* 125 (20) (2021) 11147–11158.
- [12] J. C. Simo, J. Oliver, F. Armero, *An analysis of strong discontinuities induced by strain-softening in rate-independent inelastic solids*, *Computational Mechanics* 12 (5) (1993) 277–296.

[13] M. Ortiz, A. Pandolfi, Finite-deformation irreversible cohesive elements for three-dimensional crack-propagation analysis, *International Journal for Numerical Methods in Engineering* 44 (9) (1999) 1267–1282.

[14] A. Tabarraei, J.-H. Song, H. Waisman, A two-scale strong discontinuity approach for evolution of shear bands under dynamic impact loads, *International Journal for Multiscale Computational Engineering* 11 (6) (2013).

[15] R. T. Rockafellar, S. Uryasev, Optimization of conditional value-at-risk, Vol. 2, Springer, 2000.

[16] C. Acerbi, D. Tasche, On the coherence of expected shortfall, *Journal of Banking & Finance* 26 (2002) 1487–1503.

[17] R. T. Rockafellar, S. Uryasev, Conditional value-at-risk for general loss distributions, *Journal of Banking & Finance* 26 (2002) 1443–1471.

[18] G. Pflug, Some remarks on the value-at-risk and the conditional value-at-risk, *Probabilistic Engineering Mechanics* 15 (2000) 79–86.

[19] D. Lee, B. Kramer, Bi-fidelity conditional value-at-risk estimation by dimensionally decomposed generalized polynomial chaos expansion, *Structural and Multidisciplinary Optimization* 66 (2) (2023) 33.

[20] F. Airaudo, H. Antil, R. Lohner, U. Rakhimov, On the use of risk measures in digital twins to identify weaknesses in structures, in: AIAA SCITECH 2024 Forum, 2024, p. 2622.

[21] L. J. Hong, G. Liu, Monte Carlo estimation of value-at-risk, conditional value-at-risk and their sensitivities, in: Proceedings of the Winter Simulation Conference (WSC), 2011.

[22] S. K. Au, J. L. Beck, Estimation of small failure probabilities in high dimensions by subset simulation, *Probabilistic Engineering Mechanics* 16 (4) (2001) 263–277.

[23] B. Xie, C. Peng, Y. Wang, Combined relevance vector machine technique and subset simulation importance sampling for structural reliability, *Applied Mathematical Modelling* 113 (2023) 129–143.

[24] N. E. Owen, P. Challenor, P. P. Menon, S. Ben-nani, Comparison of surrogate-based uncertainty quantification methods for computationally expensive simulators, *SIAM/ASA Journal on Uncertainty Quantification* 5 (1) (2017) 403–435.

[25] G. Blatman, B. Sudret, Adaptive sparse polynomial chaos expansion based on least angle regression, *Journal of Computational Physics* 230 (2011) 2345–2367.

[26] B. Sudret, Global sensitivity analysis using polynomial chaos expansions, *Reliability Engineering & System Safety* 93 (2008) 964–979.

[27] C. K. I. Williams, M. Seeger, Using the nyström method to speed up kernel machines, *NeurIPS* 13 (2001).

[28] C. E. Rasmussen, C. K. I. Williams, *Gaussian Processes for Machine Learning*, MIT Press, 2006.

[29] G. Brassard, P. Høyer, M. Mosca, A. Tapp, Quantum amplitude amplification and estimation, in: H.-K. Lo, T. Spiller, S. Popescu (Eds.), *Quantum Computation and Quantum Information: A Millennium Volume*, American Mathematical Society, 2002, pp. 53–74.

[30] S. Heinrich, Quantum summation with an application to integration, *Journal of Complexity* 18 (1) (2002) 1–50.

[31] A. Montanaro, Quantum speedup of monte Carlo methods, *Proceedings of the Royal Society A* 471 (2181) (2015) 20150301.

[32] S. Woerner, D. J. Egger, Quantum risk analysis, *npj Quantum Information* 5 (2019) 1–12.

[33] P. Rebentrost, K. Gupt, T. R. Bromley, Quantum computational finance: Monte Carlo pricing of financial derivatives, *Physical Review A* 98 (2018) 022321.

[34] N. Stamatopoulos, D. J. Egger, Y. Sun, S. Woerner, Option pricing using quantum computers, *Quantum* 4 (2020) 291.

[35] B. M. Austin, D. Y. Zubarev, W. A. Lester Jr, Quantum monte Carlo and related approaches, *Chemical reviews* 112 (1) (2012) 263–288.

[36] L. K. Grover, A fast quantum mechanical algorithm for database search, in: *Proceedings of the 28th Annual ACM Symposium on Theory of Computing (STOC)*, ACM, 1996, pp. 212–219.

[37] Y. Suzuki, S. Endo, S. C. Benjamin, E. G. Rieffel, P. L. McMahon, Y. Yamazaki, Amplitude estimation without phase estimation, *Quantum Information Processing* 19 (2) (2020) 75.

[38] D. Grinko, J. Gacon, C. Zoufal, S. Woerner, Iterative quantum amplitude estimation, *npj Quantum Information* 7 (2021) 52.

[39] N. Wiebe, C. Granade, Efficient bayesian phase estimation, *Physical Review Letters* 117 (1) (2016) 010503.

[40] J. He, An efficient quantum computing based structural reliability analysis method using quantum amplitude estimation, *Structural Safety* 114 (2025) 102555.

[41] A. Tabarraei, Variational quantum latent encoding for topology optimization, *Engineering with Computers* 41 (6) (2025) 4549–4573.

[42] A. Arora, B. M. Ward, C. Oskay, An implementation of the finite element method in hybrid classical/quantum computers, *Finite Elements in Analysis and Design* 248 (2025) 104354.

[43] A. Montanaro, S. Pallister, Quantum algorithms and the finite element method, *Physical Review A* 93 (3) (2016) 032324. doi:10.1103/PhysRevA.93.032324.

[44] T. Xu, H. Nguyen, M. Ortiz, Quantum computing enhanced distance-minimizing data-driven computational mechanics, *Computer Methods in Applied Mechanics and Engineering* 418 (2024) 116463. doi:10.1016/j.cma.2023.116463.

[45] J. E. Kim, Y. Wang, Variational quantum algorithm for constrained topology optimization, *Quantum Science and Technology* 10 (4) (2025) 045025.

[46] M. A. Nielsen, I. L. Chuang, *Quantum Computation and Quantum Information*, Cambridge University Press, 2010.

[47] C. J. Clopper, E. S. Pearson, The use of confidence or fiducial limits illustrated in the case of the binomial, *Biometrika* 26 (4) (1934) 404–413.

[48] L. D. Brown, T. T. Cai, A. DasGupta, Interval estimation for a binomial proportion, *Statistical Science* 16 (2) (2001) 101–133.

[49] M. Abramowitz, I. A. Stegun, *Handbook of Mathematical Functions with Formulas, Graphs, and Mathematical Tables*, Vol. 55 of *Applied Mathematics Series*, National Bureau of Standards, 1964.

[50] D. W. Lozier, Nist digital library of mathematical functions, *Annals of Mathematics and Artificial Intelligence* 38 (1) (2003) 105–119.

Appendix A. Explicit circuit-level construction of the oracle and Grover iterates: a two-qubit worked example

This appendix provides a complete circuit-level realization of the oracle A and Grover amplification operator G used throughout the paper, together with a fully worked two-qubit numerical example. The goal is to make the abstract definitions in the main text explicit by showing how scenario-dependent ancilla rotations are implemented using standard quantum gates, how the oracle-prepared state $|\Psi\rangle = A|000\rangle$ is constructed step by step, and how successive Grover iterates act on this state at the level of state vectors. We further illustrate how amplified measurement outcomes at different Grover depths are converted into confidence-consistent admissible sets for the unknown rotation angle θ using interval-based inference, and how intersections across depths progressively refine the feasible region.

Appendix A.1. Scenario-dependent ancilla rotations and block-wise action

We consider the two-qubit oracle circuit shown in Fig. 1 with index qubits (q_0, q_1) and ancilla q_2 . The oracle implements a lookup-table encoding in which each index basis state applies a prescribed rotation to the ancilla. In this example,

$$\begin{aligned} |00\rangle &: \text{no rotation,} \\ |01\rangle &: R_y(0.70), \\ |10\rangle &: R_y(1.20), \\ |11\rangle &: R_y(1.80). \end{aligned} \quad (\text{A.1})$$

We use the qubit ordering $|q_0q_1q_2\rangle$ and the basis

$$(|000\rangle, |001\rangle, |010\rangle, |011\rangle, |100\rangle, |101\rangle, |110\rangle, |111\rangle).$$

After applying Hadamard gates to the index qubits

$$\begin{aligned} |\psi_1\rangle &= (H \otimes H \otimes I)|000\rangle \\ &= \frac{1}{2} (|000\rangle + |010\rangle + |100\rangle + |110\rangle). \end{aligned} \quad (\text{A.2})$$

Ancilla rotation conditioned on the $|01\rangle$ index state.. Because the $|00\rangle$ scenario corresponds to a zero rotation, no circuit block is required for this component. The first nontrivial encoding therefore targets the $|01\rangle$ basis state and corresponds to the second block in Fig. 1. This block consists of an X gate on q_0 , followed by a doubly controlled $R_y(0.70)$ rotation on the ancilla, and a second X gate on q_0 to uncompute the pattern conversion. Together, these operations implement a control-on- $|0\rangle$ condition for q_0 and a control-on- $|1\rangle$ condition for q_1 , ensuring that the rotation is applied exclusively to the $|01\rangle$ component of the index register.

We first apply an X gate on q_0 to convert the control-on- $|0\rangle$ condition into a standard control-on- $|1\rangle$ form. The resulting state is

$$|\psi_2\rangle = (X \otimes I \otimes I)|\psi_1\rangle = \frac{1}{2} (|000\rangle + |010\rangle + |100\rangle + |110\rangle), \quad (\text{A.3})$$

which differs from $|\psi_1\rangle$ only by a permutation of basis labels, leaving all amplitudes unchanged.

Next, a doubly controlled $R_y(0.70)$ gate is applied to the ancilla. This operation acts only on the component with $(q_0, q_1) = (1, 1)$. Using

$$R_y(\theta)|0\rangle = \cos(\theta/2)|0\rangle + \sin(\theta/2)|1\rangle, \quad (\text{A.4})$$

the resulting state is

$$|\psi_3\rangle = \frac{1}{2}|000\rangle + \frac{1}{2}|010\rangle + \frac{1}{2}|100\rangle + \frac{1}{2}\cos(0.35)|110\rangle + \frac{1}{2}\sin(0.35)|111\rangle. \quad (\text{A.5})$$

Finally, the X gate on q_0 is applied again to uncompute the pattern conversion. This restores the original index labeling while preserving the ancilla rotation, yielding

$$|\psi_4\rangle = \frac{1}{2}|000\rangle + \frac{1}{2}\cos(0.35)|010\rangle + \frac{1}{2}\sin(0.35)|011\rangle + \frac{1}{2}|100\rangle + \frac{1}{2}|110\rangle. \quad (\text{A.6})$$

The corresponding state vector representation is

$$\vec{\psi}_4 = \begin{bmatrix} \frac{1}{2} \\ 0 \\ \frac{1}{2}\cos(0.35) \\ \frac{1}{2}\sin(0.35) \\ \frac{1}{2} \\ 0 \\ \frac{1}{2} \\ 0 \end{bmatrix}. \quad (\text{A.7})$$

Ancilla rotations for the $|10\rangle$ and $|11\rangle$ index states.. The Third and fourth blocks in Fig. 1 repeat the same structure to encode the remaining scenarios. Specifically,

- the $|10\rangle$ component is rotated by $R_y(1.20)$, and
- the $|11\rangle$ component is rotated by $R_y(1.80)$.

No other components are modified.

After all three blocks are applied, the oracle produces

$$\begin{aligned} |\Psi\rangle = A|000\rangle &= \frac{1}{2}(|00\rangle|0\rangle \\ &+ |01\rangle[\cos(0.35)|0\rangle + \sin(0.35)|1\rangle] \\ &+ |10\rangle[\cos(0.60)|0\rangle + \sin(0.60)|1\rangle] \\ &+ |11\rangle[\cos(0.90)|0\rangle + \sin(0.90)|1\rangle]). \end{aligned} \quad (\text{A.8})$$

In vector form,

$$\vec{\Psi} = \begin{bmatrix} \frac{1}{2} \\ 0 \\ \frac{1}{2}\cos(0.35) \\ \frac{1}{2}\sin(0.35) \\ \frac{1}{2}\cos(0.60) \\ \frac{1}{2}\sin(0.60) \\ \frac{1}{2}\cos(0.90) \\ \frac{1}{2}\sin(0.90) \end{bmatrix} \approx \begin{bmatrix} 0.500000 \\ 0.000000 \\ 0.469686 \\ 0.171449 \\ 0.412668 \\ 0.282321 \\ 0.310805 \\ 0.391663 \end{bmatrix}. \quad (\text{A.9})$$

Measuring the ancilla qubit therefore yields outcome $|1\rangle$ with probability $\sum_i p_i g_i$, consistent with the abstract oracle definition.

Appendix A.2. Grover iterate G as a circuit and continued two-qubit numerical example

The Grover iterate is defined in Eq. (35) and given by $G = -AS_0A^\dagger S_\chi$.

Operation 1: apply S_χ . Applying S_χ multiplies all amplitudes with ancilla bit $q_2 = 1$ by -1 :

$$\vec{\Psi}^{(\chi)} = S_\chi \vec{\Psi} \approx \begin{bmatrix} 0.500000 \\ 0.000000 \\ 0.469686 \\ -0.171449 \\ 0.412668 \\ -0.282321 \\ 0.310805 \\ -0.391663 \end{bmatrix}. \quad (\text{A.10})$$

Operation 2: apply A^\dagger . Next, uncompute using A^\dagger

$$\vec{v} = A^\dagger \vec{\Psi}^{(\chi)}. \quad (\text{A.11})$$

Since A consists of Hadamards on (q_0, q_1) and scenario-controlled R_y rotations on q_2 , A^\dagger is implemented by reversing the same circuit and replacing each $R_y(\theta)$ by $R_y(-\theta)$. For this example, the resulting vector is (numerically, to 6 digits)

$$\vec{v} \approx \begin{bmatrix} 0.474999 \\ -0.637526 \\ 0.206179 \\ 0.171507 \\ 0.407422 \\ 0.315417 \\ -0.088601 \\ 0.150602 \end{bmatrix}. \quad (\text{A.12})$$

Operation 3: apply S_0 . The reflection $S_0 = I - 2|000\rangle\langle 000|$ flips the sign of the $|000\rangle$ amplitude only:

$$\vec{v}^{(0)} = S_0 \vec{v} \approx \begin{bmatrix} -0.474999 \\ -0.637526 \\ 0.206179 \\ 0.171507 \\ 0.407422 \\ 0.315417 \\ -0.088601 \\ 0.150602 \end{bmatrix}. \quad (\text{A.13})$$

Operation 4: apply A (complete one Grover iterate). Finally,

$$\vec{\Psi}^{(G)} = -A \vec{v}^{(0)}. \quad (\text{A.14})$$

Carrying out the multiplication yields

$$\vec{\Psi}^{(G)} \approx \begin{bmatrix} -0.025001 \\ 0.000000 \\ -0.023485 \\ 0.334325 \\ -0.020634 \\ 0.550526 \\ -0.015541 \\ 0.763743 \end{bmatrix}. \quad (\text{A.15})$$

Amplified success probability p_1 . Success corresponds to ancilla $q_2 = 1$, i.e. basis states $|001\rangle, |011\rangle, |101\rangle, |111\rangle$ (entries 2,4,6,8 in our ordering). Thus,

$$\begin{aligned} p_1 &= |(\vec{\Psi}^{(G)})_{001}|^2 + |(\vec{\Psi}^{(G)})_{011}|^2 \\ &\quad + |(\vec{\Psi}^{(G)})_{101}|^2 + |(\vec{\Psi}^{(G)})_{111}|^2 \\ &\approx (0.000000)^2 + (0.334325)^2 \\ &\quad + (0.550526)^2 + (0.763743)^2 \approx 0.998156. \end{aligned} \quad (\text{A.16})$$

Check against amplitude-amplification theory. The unamplified success probability is obtained from $|\Psi\rangle = A|000\rangle$: For the oracle-prepared state $|\Psi\rangle = A|000\rangle$, the unamplified success probability is

$$\begin{aligned} a &= p_0 = \frac{1}{4}(\sin^2(0.35) + \sin^2(0.60) + \sin^2(0.90)) \\ &\approx 0.262500. \end{aligned} \quad (\text{A.17})$$

Writing $a = \sin^2 \theta$ gives $\theta \approx 0.537916$, and the Grover prediction is

$$p_1 = \sin^2(3\theta) \approx 0.998156,$$

which matches Eq. (A.16).

Appendix A.3. Numerical illustration of interval-based inference for $k = 0$ and $k = 1$

At depth $k = 0$, the success probability satisfies $p_0(\theta) = \sin^2 \theta$. Suppose the amplified circuit is executed $m_0 = 1000$ times and $h_0 = 262$ successes are observed, corresponding to an empirical frequency $\hat{p}_0 = 0.262$.

Using the Clopper–Pearson construction defined in Section 4.2.1, the resulting confidence interval for p_0 is

$$p_0 \in [0.23498, 0.29043]. \quad (\text{A.18})$$

Since $\sin^2 \theta$ is monotone on $(0, \pi/2)$, this interval maps uniquely to an admissible interval for θ :

$$\begin{aligned} \Theta_0 &= [\arcsin(\sqrt{0.23498}), \arcsin(\sqrt{0.29043})] \\ &= [0.50607, 0.56915] \text{ rad.} \end{aligned} \quad (\text{A.19})$$

At depth $k = 1$, the response function is $p_1(\theta) = \sin^2(3\theta)$. Suppose that $m_1 = 1000$ executions yield $h_1 = 998$ successes, corresponding to $\hat{p}_1 = 0.998$. The associated Clopper–Pearson confidence interval is

$$p_1 \in [0.99279, 0.99976]. \quad (\text{A.20})$$

Following the interval-to-angle mapping described in Section 4.2.2, this probability interval induces two admissible branches for θ on $(0, \pi/2)$:

$$\Theta_1 = [0.49527, 0.51841] \cup [0.52879, 0.55193] \text{ rad.} \quad (\text{A.21})$$

The presence of two disjoint intervals reflects the non-injective nature of the mapping $\theta \mapsto \sin^2(3\theta)$.

Appendix A.4. Intersection of admissible sets

Combining information from depths $k = 0$ and $k = 1$ corresponds to intersecting the admissible sets Θ_0 and Θ_1

$$\begin{aligned} \Theta^{(1)} &= \Theta_0 \cap \Theta_1 \\ &= [0.50607, 0.51841] \cup [0.52879, 0.55193] \text{ rad.} \end{aligned} \quad (\text{A.22})$$

Thus, after two rounds, the feasible region consists of two remaining hypotheses. In the full ML-IQAE procedure, additional Grover depths or scheduled disambiguation rounds are used to eliminate spurious branches and isolate a single confidence-consistent interval for θ . Once a unique interval is identified, bounds or point estimates for the amplitude $a = \sin^2 \theta$ follow immediately.